Palaeogeography, Palaeoclimatology, Palaeoecology 634 (2024) 111958

Contents lists available at ScienceDirect

Palaeogeography, Palaeoclimatology, Palaeoecology

journal homepage: www.elsevier.com/locate/palaeo

Natural and anthropogenic forcing on the fate of sedimentary organic matter in the South Yellow Sea during the Holocene

Chuchu Zhang [a,b,c], Yifei Qiu [a], Zhi Dong [d], Chenglong Wang [a,b,*], Yameng Wang [a,b,c], Qihang Liao [a,b,c], Xinqing Zou [a,b,c,*]

[a] School of Geographic and Oceanographic Sciences, Nanjing University, Nanjing 210093, China
[b] Ministry of Education Key Laboratory for Coast and Island Development, Nanjing University, Nanjing 210093, China
[c] Collaborative Innovation Center of South China Sea Studies, Nanjing University, Nanjing 210093, China
[d] Key Laboratory of Marine Geology and Metallogeny, First Institute of Oceanography, Ministry of Natural Resources, Qingdao 266061, China

ARTICLE INFO

Editor: M Zhao

Keywords:
Sedimentary organic matter
South Yellow Sea
Holocene
Climate change
Human activities

ABSTRACT

Long-term organic matter (OM) burial in the ocean is essential to the global carbon cycle. Mud deposits, such as South Yellow Sea mud deposit (SYSMD) located in the central South Yellow Sea (SYS), are ideal for the study of long-term OM burial. A sediment core YS-A from the SYSMD was analyzed for lignin phenols and bulk OM properties to reveal the driving forces of sedimentary OM (SOM) fate during the Holocene. SOM burial was found to be dominantly influenced by sea level rise and increased East Asian summer monsoon during 11.0–7.0 ka BP. During 7.0–1.0 ka BP, the fate of SOM was controlled by El Niño Southern Oscillation on the millennial time scale, and correlated with East Asian winter monsoon variability on the centennial time scale. Remarkably, anthropogenic perturbation has gradually overwhelmed long-term climate control on the fate of SOM since 1.0 ka BP, and this phenomenon became more evident after 0.4 ka BP.

1. Introduction

Oceans are an important carbon sink, with the long-term storage of organic matter (OM) in marine sediments playing a key role in the carbon cycle of earth (Berner, 1990; Burdige, 2005). Particularly, ocean margins bury >80% of the global sedimentary OM (SOM), despite occupying <8% of the global ocean area (Berner, 1982; Hedges and Keil, 1995). As the transition zone connecting the continent to the ocean, the high flux and efficiency of SOM burial in ocean margins can be attributed to high terrestrial OM (TOM) inputs, phytoplankton productivity, and sedimentation rates (McKee et al., 2004; Burdige, 2005). The processes governing the fate of SOM in ocean margins, including its delivery, dispersal, degradation, and burial (Bianchi, 2011; Wang et al., 2020), has attracted the attention of scientists for decades and significantly influences the elucidation of the global carbon cycle.

Previous studies have focused on global OM burial at different time periods such as centennium (Cuellar-Martinez et al., 2020; Pellegrini et al., 2021), millennium (Samper-Villarreal et al., 2018; Schwestermann et al., 2021) and even longer timescales (Bodin et al., 2015; Hartke et al., 2021; Raven et al., 2023). However, there have been limited investigations specifically focused on the Holocene, a special geological period affected by climate change and anthropogenic activities. The drastic climate variabilities during the Holocene inevitably affected terrestrial input and marine primary productivity (Pu et al., 2013; Wang et al., 2021), and eventually affected the burial of SOM in ocean margins. Notably, since the Late Holocene, the increase in population has led to enhanced cultivation and deforestation (Milliman et al., 1987; Ren and Zhu, 1994), which have triggered massive terrestrial inputs and affected SOM burial in ocean margins. Therefore, the fate of SOM in ocean margins during the Holocene should be determined to elucidate the carbon cycle in geological history and its future development trend.

The eastern Chinese marginal seas are typical ocean margins on earth resulting from huge amount of terrestrial input, which bury approximately 10% of SOM in global ocean margins (Deng et al., 2006; Hu et al., 2016). Numerous researches have focused on the source, transportation, degradation, and burial of SOM in modern sediments (Bao et al., 2016; Zhao et al., 2021), and certain studies have explored the fate of SOM on the centennial scale (Liu et al., 2013; Wang et al., 2021). These studies found climate variability and anthropogenic perturbation as the main

* Corresponding authors at: School of Geographic and Oceanographic Sciences, Nanjing University, Nanjing 210093, China.
E-mail addresses: clwang@nju.edu.cn (C. Wang), zouxq@nju.edu.cn (X. Zou).

https://doi.org/10.1016/j.palaeo.2023.111958
Received 12 June 2023; Received in revised form 29 November 2023; Accepted 1 December 2023
Available online 2 December 2023

possible factors influencing the fate of SOM in eastern Chinese marginal seas (Wang et al., 2021; Wang et al., 2022). Mud deposits, such as South Yellow Sea mud deposit (SYSMD) located in the central South Yellow Sea (SYS), are ideal for the study of long-term OM burial (Fig. 1a). The SYSMD is significant to the study of Holocene climate change and human activities (Hao et al., 2017; Ai et al., 2022), but only a few studies have focused on SOM burial during the Holocene. Two types of indicators are presently used for estimating the fate of organic material in sediments: bulk source indicators (C/N values, carbon and nitrogen stable isotopic composition) and organic matter biomarkers (lignins, straight chain aliphatic hydrocarbons and glycerol dialkyl glycerol tetraethers). Lignins are exclusively present in vascular plants and highly resistant to degradation, making them an ideal tracer of TOM (Xu et al., 2009). Previous studies used lignin phenols of sediment cores in the SYSMD as climate indicators since 7.0 ka BP (Gong et al., 2017; Hao et al., 2017). In this study, lignin phenols and bulk OM properties were analyzed to describe the source, degradation, and burial of SOM in the SYSMD during different periods of Holocene. Parameters related to climate change (e.g., the intensity of the East Asian summer monsoon (EASM), East Asian winter monsoon (EAWM) and frequency of El Nino-Southern Oscillation (ENSO)) and human activities (including population, sediment loads, and tree cover) were used to determine the key factors affecting the fate of SOM during the Holocene.

2. Material and methods

2.1. Material

The SYS is a typical river-dominated ocean margin, that received large amounts of sediments from the Yellow River. The sea level of the SYS at 11.0 ka BP was approximately 40 m below the present level (Liu et al., 2004). At this stage, the paleo-Yellow River was deduced to enter the SYS at the Bohai Strait and to develop a proximal subaqueous delta along the northern coast of the Shandong Peninsula (Yang and Liu, 2007). At approximately 7.0–6.0 ka BP, the sea level reached its highest level and stabilized, and the Yellow River estuary receded to its present position following transgression. The modern circulation system consisting of the Yellow Sea Warm Current (YSWC), the Yellow Sea Coastal Current (YSCC), and the Korean Coastal Current (KCC) was formed (Fig. 1b; Yuan et al., 2008; Moon et al., 2009). Meanwhile, the SYSMD gradually developed owing to the trapping effect of the modern circulation system (Yang et al., 2003), and undergone a two-phase process of "storage in summer and transportation in winter". The sediment core YS-A (122.9°N, 36.3°E) was collected from the SYSMD (Fig. 1b) in the November of 2019. The water depth of YS-A is 64.8 m and the length of core is 240 cm. The core was subsampled at 1 cm intervals to yield 240 sediment samples and stored at −20 °C.

2.2. Methods

2.2.1. Core lithology and chronology

The age model of core YS-A was obtained by accelerator mass spectrometry (AMS) ^{14}C dating of twelve mixed benthic foraminifera at Pilot National Laboratory for Marine Science and Technology (Qingdao). All dates were calibrated to calendar years before "present" (before 1950 CE, or BP) using the CALIB 8.20 program with an updated calibration curve Marine20. The correction factor Delta $R = -173 \pm 88$ yr, which was obtained from 10 nearest data points from Qingdao, Korean peninsula, Busan, Okinawa and Amani-Oshima (Southon et al., 2002; Kong and Lee, 2005; Yoneda et al., 2007; Kim et al., 2021). To optimize the available dates, age-depth modeling was carried out by Bayesian analysis using the Bacon program in R (Blaauw and Christen, 2011).

2.2.2. Grain size

Grain size analyses were measured with a laser diffraction particle size analyzer (Mastersizer 2000, Malven Instruments Ltd., UK) from 0.02 to 2000 μm. The measuring error was within 3%. All the samples were

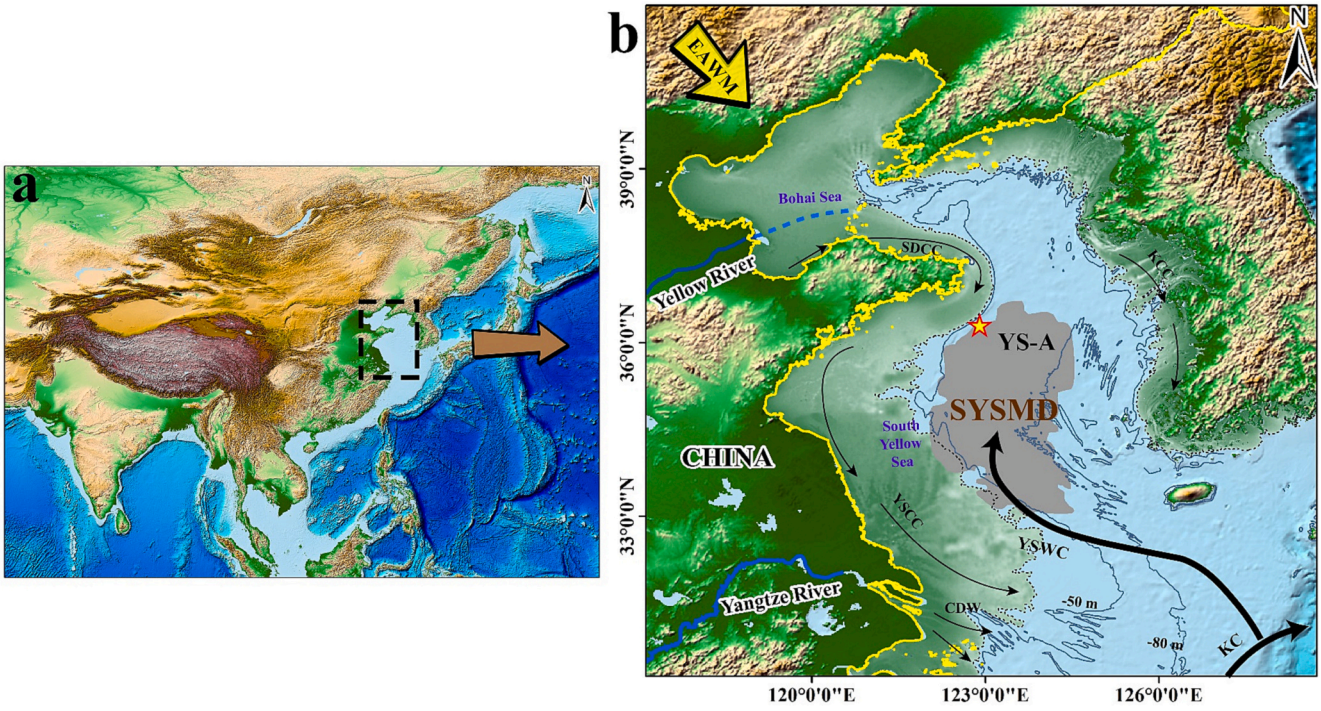

Fig. 1. Map showing the study area, location of core YS-A (yellow pentagram) and surface current system (black arrows) around the area. The coastline was moved to the approximate position of present 40 m isobaths at 11.0 ka BP (the palo and present coastline is shown in black dotted line and yellow line), and proximal subaqueous delta along the northern coast of the Shandong Peninsula (light green area) developed. The blue dashed line indicates the possible location of the Paleo-Yellow River estuary. Dark grey area indicates the South Yellow Sea mud deposit (SYSMD). (For interpretation of the references to colour in this figure legend, the reader is referred to the web version of this article.)

washed with 10% H_2O_2 and 1 mol/L HCl for 24 h to remove the organic matter and biogenic carbonate, and immersed in sodium metaphosphate for 24 h prior to grain-size analyses. According to the Folk classification system, the grain sizes were divided into clay (< 4 μm), silt (4–63 μm) and sand (> 63 μm).

2.2.3. Bulk Parameters

All the sediment samples were analyzed for total organic carbon (TOC), total nitrogen (TN) and their stable isotopes, following the methods described by Xing et al. (2011). The freeze-dried and homogenized samples were treated with 1 M HCl to remove inorganic carbon, and then rinsed several times with deionized water to neutralize them. A Thermo Flash 2000 elemental analyzer interfaced with a MAT253 isotope ratio mass spectrometer was used to determine the TOC, TN content and stable isotopes.

2.2.4. Lignin phenols

Lignin analysis was carried out by a modified method based on the conventional alkaline CuO oxidations as described by Yu et al. (2011). About 1 g of freeze-dried sediment, 1 g CuO and 0.05 g Fe $(NH_4)_2(SO_4)_2{\cdot}6H_2O$ was placed in a Teflon reaction vessel and 15 mL 2 M NaOH was added to the vessel in a glove box filled with N_2.Then the vessel was placed in an incubator at 170 °C for 3 h. After cooling down, recovery standards (ethyl vanillin and trans-cinnamic acid) were added to the alkaline solutions and then acidified to pH 1 with concentrated HCl. Samples were extracted by using a Cleanert PEP-SPE column (500 mg, Agela Technologies), eluted with ethyl acetate, dried with N_2 and dissolved in acetonitrile. Prior to analysis, the sample was derivatized with bis-trimethylsilyl-trifluoroacetamide plus 1% trimethylchlorosilane (BSTFA+1%TMCS) at 60 °C for 1 h.

CuO oxidation products analysis were analyzed by Gas Chromatography coupled with Flame Ionization Detector (GC/FID), fitted with a quartz capillary TG-5MS column (30 m × 0.25 mm × 0.25 μm film thickness). The GC temperature was initially set at 100 °C and held for 1 min, finally increased to 290 °C at a 4 °C/min rate. Helium was used as the carrier gas with a flow rate of 1.5 mL/min. The lignin components were identified based on the retention time of corresponding individual standards, and their quantification was carried out based on the eight-point standard curves.

Lignin phenols used as molecular indicators included three vanillyl phenols (V: vanillin, acetovanillone, and vanillic acid), three syringyl phenols (S: syringaldehyde, acetosyringone, and syringic acid, two cinnamyl phenols (C: p-coumaric acid and ferulic acid), Other compounds derived from the CuO oxidation used as molecular indicators included three p-hydroxy phenols (P: p-hydroxybenzaldehyde, p-hydroxyace-tophenone, and p-hydroxybenzoic acid). The Σ8 (mg/10 g ds) and Λ8 (mg/100 mg OC) are the concentrations of 8 major lignin phenols (S + V + C) relative to 10 g dry sediment (ds) and normalized to 100 mg of OC, respectively.

2.2.5. Three end-member mixing models

In this study, we used three end-member mixing model to distinguish different sources of OC. The three end-member mixing model based on a Monte Carlo simulation approach using $\delta^{13}C$ and Λ8 as source markers was employed to distinguish the relative contributions of plant OC, soil OC and marine OC in the core YS-A (Andersson, 2011):

$$\Lambda 8_{sample} = f_{plant} \times \Lambda 8_{plant} + f_{soil} \times \Lambda 8_{soil} + f_{marine} \times \Lambda 8_{marine} \quad (1)$$

$$\delta^{13}C_{sample} = f_{plant} \times \delta^{13}C_{plant} + f_{soil} \times \delta^{13}C_{soil} + f_{marine} \times \delta^{13}C_{marine} \quad (2)$$

$$f_{plant} + f_{soil} + f_{marine} = 1 \quad (3)$$

where, f_{plant}, f_{soil}, and f_{marine} are the relative contributions of vascular plant OC, soil OC and marine OC, and the $\Lambda 8_{sample}$ and $\delta^{13}C_{sample}$ are measured Λ8 and $\delta^{13}C$ values in sediment samples, respectively.

Λ8 of typical C3 vascular plants in the Changjiang basin were used as the end-member values due to lack of data from the Yellow River basin (Zhao et al., 2021). This is reasonable because the $\delta^{13}C$ values of vascular plant OC in the Changjiang basin (−28.10 ± 1.68‰) (Yu et al., 2007) is within the same range as C3 plants from the Loess Plateau (−26.7 ± 4.18‰) (Wang et al., 2003), which is the major particulate matter source to the Yellow River. And Λ8 values of surface sediments in Yellow Sea (0.98 ± 0.92 mg/100 mg OC) and East Sea (0.86 ± 0.23 mg/100 mg OC) were fairly close (Zhang, 2012). Therefore, the end-member values of vascular plant OC for $\delta^{13}C$ and Λ8 were − 26.7 ± 4.18‰ and 6.00 ± 5.22 mg/100 mg OC (Wang et al., 2003; Yu et al., 2007). The average values of riverbank soil samples from the whole basins of Yellow River were used as soil end-member values ($\delta^{13}C_{soil}$ = −24.86 ± 0.94‰ and $\Lambda 8_{soil}$ = 2.37 ± 2.00 mg/100 mg OC) (Yu et al., 2007; Gao et al., 2016). The end-member values of marine OC for $\delta^{13}C$ and Λ8 were − 20.0 ± 1.0‰ and 0 mg/100 mg OC, respectively (Wang et al., 2015; Zhang et al., 2007).

2.2.6. Statistical analysis

Pearson correlation and a two-tailed test of significance were performed to determine relationships between the measured parameters using IBM SPSS Statistics 24.0. The Monte Carlo simulation was applied by a Matlab script (Version R2020b, Math Works) (Andersson, 2011). This model used end-member values of $\delta^{13}C$ and Λ8, with the average value and standard deviation following a normal distribution. For each sample, 1,000,000 out of 100, 000, 000 random samples from the normal distribution of end-member value were taken for the above equations (Eqs. (1)–(3)). The details of simulation process were shown in Li et al. (2014).

3. Results

3.1. Chronology

The AMS ^{14}C dating is based on twelve mixed benthic foraminifera samples, which are shown in Table 1. The age-depth model of core YS-A determined using Bayesian analysis and Bacon program for R is shown in Fig. 2. Our age model shows that the 240 cm section of the core YS-A covers the 10,955 cal yr BP period. The average sediment accumulation rates and resolution were approximately 21.91 cm/kyr and 46 yr/cm.

3.2. Grain size and bulk properties

Sand, silt, and clay content in this core ranged from 0.00 to 6.33%, 48.54–74.89%, and 24.42–51.36%, with average values of 1.03 ± 1.34%, 62.04 ± 4.96%, and 36.94 ± 5.12%, respectively (Fig. S1a). The mean grain size ranged from 4.12 to 9.12 μm, with a mean value of 6.09 ± 0.97 μm (Fig. S1b). The sand fraction decreased from 240 to 180 cm, and was almost absent from 180 cm to the top (Fig. S1a). The silt and clay fractions showed a consistent slight increase from 240 to 180 cm, corresponding to the decreasing trend of the mean grain size (Fig. S1a, b). The mean grain size and slit fraction increased from 180 to 160 cm and decreased from 160 to 94 cm; the clay fraction showed the opposite trend (Fig. S1a, b). From 94 cm to the top, the mean grain size exhibited a fluctuant increasing trend with increasing slit fraction and decreasing clay fraction.

The TOC and TN values ranged from 0.57% to 1.53% and 0.05% to 0.18%, with mean values of 0.96 ± 0.13% and 0.12 ± 0.02% (Fig. S1c, d). TOC and TN contents displayed a positive correlation ($r = 0.88$, $p < 0.001$), suggesting that they had similar origins. The $\delta^{13}C$ values and C/N ratios ranged from −24.79‰ to −22.11‰ and 6.74 to 11.05, with a mean value of −23.13 ± 0.57‰ and 8.39 ± 0.91 (Fig. S1e, f). $\delta^{13}C$ values and C/N ratios displayed a negative correlation ($r = -0.87$, $p < 0.001$), indicating that both proxies were useful for determining the source of SOM. TOC content had a minimum value and showed an

Table 1
AMS^{14}C dating and age model of sediment core YS-A.

Core depth (cm)	Lab code	Material	AMS^{14}C age (yr BP)	Calibrated age (cal yr BP)	Calibrated age range (cal yr BP)
0	QNLMA 230131	Mixed benthic foraminifera	410 ± 30	0	–
10	QNLMA 230132	Mixed benthic foraminifera	775 ± 25	395	173–596
20	QNLMA 230133	Mixed benthic foraminifera	1155 ± 20	724	531–922
40	QNLMA 230134	Mixed benthic foraminifera	1545 ± 20	1112	895–1317
60	QNLMA 200522	Mixed benthic foraminifera	2290 ± 70	1939	1644–2274
90	QNLMA 230135	Mixed benthic foraminifera	2630 ± 20	2372	2109–2667
120	QNLMA 200523	Mixed benthic foraminifera	3615 ± 40	3562	3301–3849
140	QNLMA 230136	Mixed benthic foraminifera	4185 ± 30	4303	3997–4587
160	QNLMA 230137	Mixed benthic foraminifera	5350 ± 30	5712	5467–5939
180	QNLMA 200616	Mixed benthic foraminifera	6670 ± 40	7153	6902–7397
210	QNLMA 230138	Mixed benthic foraminifera	9700 ± 30	10,697	10,393–11,057
240	QNLMA 200617	Mixed benthic foraminifera	9890 ± 50	10,955	10,802–11,122

increasing trend in the bottom part of the core (240–180 cm), maintained a relatively high value from 180 to 130 cm, and decreased from 130 to 104 cm. Afterwards, it exhibited periodical fluctuation with high values ranging between 91 and 78 cm and 44–30 cm, and notably increased from 30 cm to the top (Fig. S1c). The $\delta^{13}C$ values were relatively negative from 240 to 180 cm, and slightly tended towards positive values as they approached 90 cm, towards negative values from 90 to 80 cm, and towards positive values from 80 to 30 cm; finally they decreased drastically towards the top (Fig. S1e). C/N ratios were relatively high from 240 to 180 cm, and then decreased slightly towards the top with relatively high values from 91 to 78 cm (Fig. S1f).

3.3. Lignin phenols

The Σ8 values ranged from 0.08 to 0.22 mg/10 g ds (dry sediment) with an average value of 0.14 ± 0.02 mg/10 g ds (Fig. S2a). The value of Σ8 increased initially at the bottom (240–180 cm), remained relatively high value from 180 to 144 cm, decreased at 143 to 94 cm, fluctuated with high values between 91 and 78 cm and 44–30 cm, and notably increased from 30 cm towards to the top. The Λ8 values ranged from 0.09 to 0.21 mg/100 mg OC, with an average value of 0.15 ± 0.02 mg/100 mg OC (Fig. S2b). A positive relationship was observed between Σ8 and Λ8 ($r = 0.55$, $p < 0.001$), but Λ8 had relatively high values and decreased from 240 to 180 cm, which is opposite to Σ8. Additionally, Λ8 had no obvious upward trend from 30 cm towards the top.

The non-lignin phenols (P) exhibited the highest content; for lignin phenols, S phenols were the highest followed by V and C phenols (Fig. S3). The P phenols content ranged from 0.05 to 0.16 mg/10 g ds with an average value of 0.09 ± 0.02 mg/10 g ds (Fig. S3a). S, V and C phenols content ranged from 0.04 to 0.11 mg/10 g ds, 0.03 to 0.07 mg/10 g ds and 0.01 to 0.03 mg/10 g ds (Fig. S3b–d), with average values of 0.07 ± 0.01 mg/10 g ds, 0.05 ± 0.01 mg/10 g ds and 0.02 ± 0.00 mg/10 g ds, respectively. S was overwhelmingly dominant in lignin content, which means that angiosperms are the main contributors to the TOM of YS-A sediments. Pon/P ratios ranged from 0.02 to 0.18 with an average value of 0.09 ± 0.02 (Fig. S2c). The low Pon/P ratios indicated that P phenols were dominantly derived from plankton or other lignin-free materials, and scarcely from vascular plants (Houel et al., 2006).

The S/V and C/V ratios ranged from 1.04 to 2.31 (Fig. S2d) and from 0.22 to 0.77 (Fig. S2e), with an average value of 1.59 ± 0.27 and 0.46 ± 0.10. Their vertical distribution had similar tendency ($r = 0.65$, $p < 0.001$). The lignin-phenol vegetation index (LPVI) values ranged from 127 to 1857, with an average of 614 (Fig. S2f). The LPVI value is strongly correlated with S/V ($r = 0.80$, $p < 0.001$) and C/V ($r = 0.96$, $p < 0.001$). S/V, C/V, and LPVI increased slightly from 240 to 180 cm, and yielded relatively high values from 151 to 71 cm throughout the core. $(Ad/Al)_V$ and $(Ad/Al)_S$ are the acid-to-aldehyde ratios of V and S phenols, respectively (Hedges et al., 1988; Dittmar and Lara, 2001). The ratios of $(Ad/Al)_V$, $(Ad/Al)_S$, and 3,5-Bd/V were used to characterize the degradation or humification state of lignin tissues. In this core, positive correlations were observed between the variations of $(Ad/Al)_V$ and $(Ad/Al)_S$ ($r = 0.39$, $p < 0.01$). $(Ad/Al)_V$ ratios ranged from 0.19 to 1.06 with an average of 0.43 ± 0.15, which increased slightly from 240 to 180 cm, and yielded relatively high values from 150 to 110 cm throughout the core (Fig. S3e). $(Ad/Al)_S$ ratios ranged from 0.33 to 1.13 with an average of 0.83 ± 0.16. They showed increasing trends from 240 to 180 cm, and were highest from 150 to 80 cm throughout the core (Fig. S3f). The 3,5-Bd/V ratios ranged from 0.02 to 0.27 with an average of 0.15 ± 0.05; they yielded the lowest values and showed increasing trends from 240 to 180 cm, then stayed relatively stable at high values towards the surface sediment (Fig. S3g).

4. Discussion

4.1. Source and degradation of SOM

Bulk OM properties such as $\delta^{13}C$ values and C/N ratios are commonly used to describe the source of SOM, because TOM has more negative $\delta^{13}C$ values and higher C/N ratios than marine organic matter (MOM). Marine algae have C/N values that range from 4 to 10 (Meyers, 1994), and the C/N ratios of C3 plants are approximately 12 or more (Tyson, 1995), whereas that of C4 plants are typically 30 or more (Meyers, 1994). $\delta^{13}C$ values of marine algae range from −19‰ to −21‰ (Fry and Sherr, 1984). Typically, C3 and C4 plants have $\delta^{13}C$ values ranging from −24‰ to −32‰ and from −9‰ to −17‰, with average values of −13‰ and − 27‰, respectively (Meyers, 1997; Lamb et al., 2006). Therefore, $\delta^{13}C$ values (−24.79 to −22.11‰) and C/N ratios (6.74–11.05) in core YS-A (Fig. 3a) suggest the contribution from both TOM and MOM.

The S/V, C/V ratios and LPVI values are used to characterize the vegetation sources in basin. S/V is used to distinguish lignin from gymnosperms (~0) or angiosperms (0.6–40); C/V is used to distinguish herbaceous tissues (> 0.20) from woody tissues (< 0.05; Goñi et al., 1998; Bianchi et al., 2011). The S/V and C/V ratios ranged from 1.04 to 2.31 and 0.22 to 0.77 (Fig. 3b), with an average value of 1.59 ± 0.27 and 0.46 ± 0.10 in this core YS-A. The combined S/V and C/V values indicate that non-woody angiosperm tissues dominated TOM in this study (Fig. 3b). LPVI values varied from approximately 1, 3–27, 67–415, and 176–2782 for gymnosperms, non-woody gymnosperms, angiosperms, and nonwoody angiosperm tissues, respectively, which are relatively sensitive to past vegetation change (Tareq et al., 2011). The values of LPVI ranged from 127 to 1857, with an average of 614 (Fig. S2f), which indicates that non-woody angiosperms tissues dominate the TOM in this core, which is similar to the interpretation of S/V and C/V.

Results of the three end-member model showed that the proportion

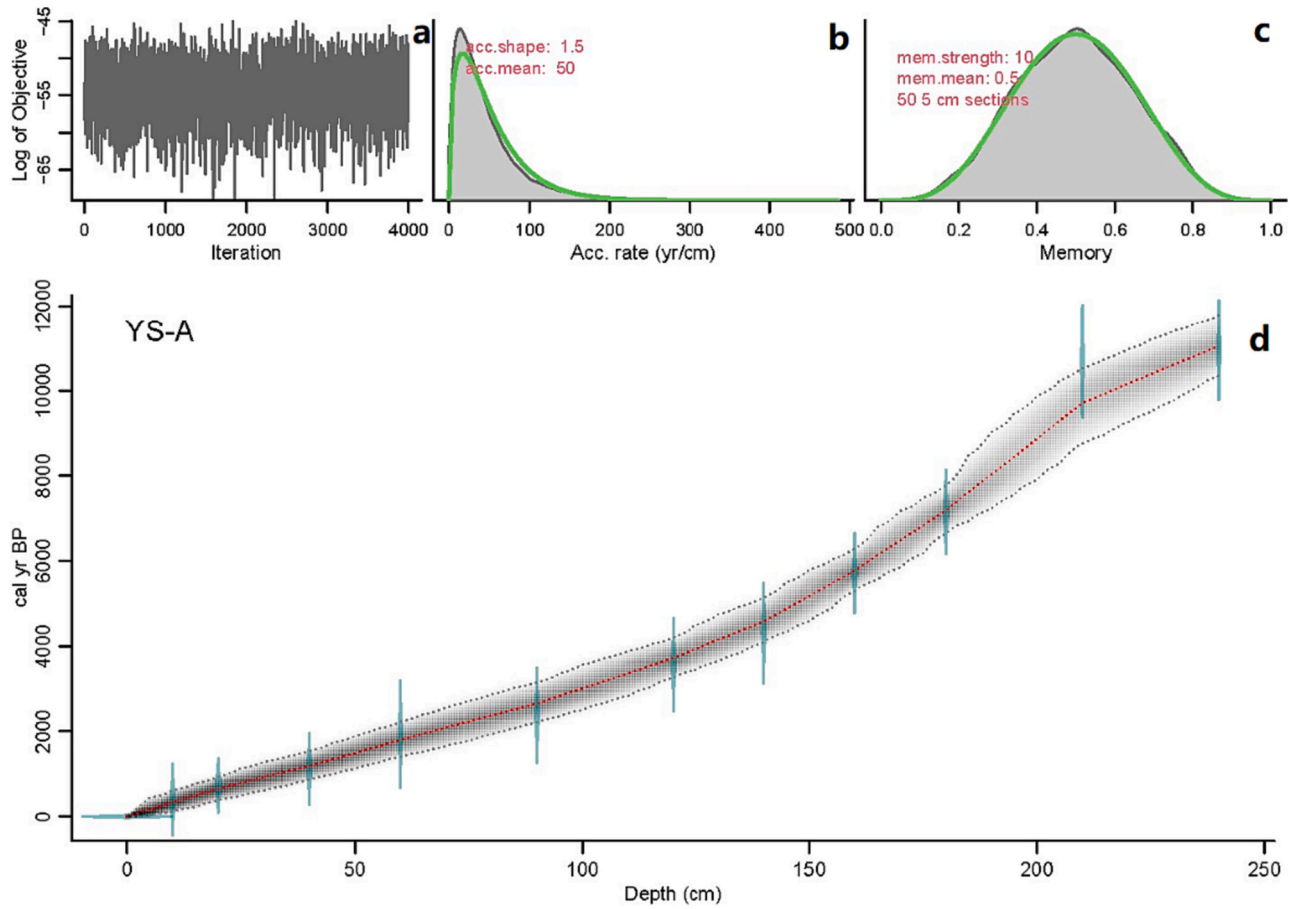

Fig. 2. Age-depth model of core YS-A determined using Bayesian analysis and Bacon program for R (Blaauw and Christen, 2011) showing: a, number of Markov Chain Monte Carlo (MCMC) iterations used to generate the grey-scale graphs; b, prior (green) and posterior (grey) distributions of the sediment accumulation rates; c, prior (green) and posterior (grey) distributions of memory; d, calibrated ^{14}C dates (green) and the age-depth model (darker grey shade represents the more probable calendar ages; grey stippled lines represent 95% confidence intervals; red stippled line indicates the best model). (For interpretation of the references to colour in this figure legend, the reader is referred to the web version of this article.)

of vascular plant OM ranged from 7.27% to 22.42% with a mean of 11.99 ± 3.04% (Fig. 4b), the proportion of soil OM ranged from 21.16% to 46.89% with an average of 34.20 ± 6.89% (Fig. 4b) and marine OM ranged from 30.90% to 71.58% with a mean of 53.82 ± 9.87% (Fig. 4c). The TOM (f_{plant} and f_{soil}) contribution of core YS-A was high and showed a decreasing trend during 11.0–7.0 ka BP (Fig. 4c), because the sea level rise caused directly effect of the Yellow River reduced in this period. Meanwhile, the f_{marine} yielded low values with increasing trends (Fig. 4c), which was probably related to the gradual recovery of marine production. Thereafter, TOM decreased slightly during 7.0–1.0 ka BP (Fig. 4c), and exhibited a drastic increasing trend 1.0 ka BP onwards (Fig. 4c).

The ratios of $(Ad/Al)_V$, $(Ad/Al)_S$ and 3,5-Bd/V are usually used to characterize the degradation of lignin tissues, and their values increase as the degree of microbial degradation increases. As V are present in all vascular plants, $(Ad/Al)_V$ ratios are more sensitive than $(Ad/Al)_S$ in determining the extent of lignin oxidative degradation (Hedges et al., 1988). $(Ad/Al)_V$ values for fresh plant tissue range from 0.1 to 0.3, and for highly degraded lignin exceeds 0.6 (Dittmar and Lara, 2001). For this core, $(Ad/Al)_V$ ratios ranged from 0.19 to 1.06 with an average of 0.43 ± 0.15 (Fig. 4d), which indicated that TOM in this core underwent a moderate to high degree of microbial degradation. Furthermore, 3,5-Bd/V values reveal the degree of humification of soil organic matter, generally <0.02 for fresh plant debris, 0.12–0.13 for peat, < 0.4 for surface soils, and 0.4–1.5 for subsurface or mineral soil (Kuzyk et al., 2008). In core YS-A, 3,5-Bd/V ratios ranged from 0.02 to 0.27 with an average of 0.15 ± 0.05 (Fig. S3g), indicating that peat and surface soils with some degree of humification made a non-negligible contribution to TOM. Notably, no trend of downcore increasing values were noted for these three degradation parameters, which is consistent with previous studies in the SYSMD (Gong et al., 2017; Hao et al., 2017). Thus, the high values of degradation parameters were better attributed to the offshore transport of degraded TOM instead of further lignin degradation after sedimentation.

4.2. Sea level and EASM control the fate of SOM during 11.0–7.0 ka BP

During 11.0–7.0 ka BP, sediment had a relatively large mean grain size, high sand content, low TOC content, and high TOM contribution (Fig. 5a–e). A positive correlation between TOC and grain size ($r = -0.81, p < 0.001$) indicates that hydrodynamics sorting affected the fate of SOM during this period (Fig. S4). The sea level of the SYSMD at 11.0 ka BP was approximately 40 m below the present level and then rapidly rose to its present level at approximately 7.0 ka BP (Fig. 5f; Liu et al., 2004). Therefore, the sedimentary environment of the SYSMD gradually transitioned from nearshore shallow sea to the present semi-closed shelf sea (Fig. 1b). The gradually finer grain size, reduced sand content, and relatively inferior sorting (Fig. 5a, b) correspond to the sea level rise during 11.0–7.0 ka BP (Fig. 5f). As the temperature and sea level increased during this period (Fig. 5f, g), marine primary productivity increased, and the sedimentary environment gradually stabilized, which allowed burial of SOM (Fig. 5c; Sun et al., 2011; Wu et al., 2019).

The results of lignin phenols showed relatively low terrestrial input with slight variation at around 11.0–8.5 ka BP (Fig. 5d). Despite the

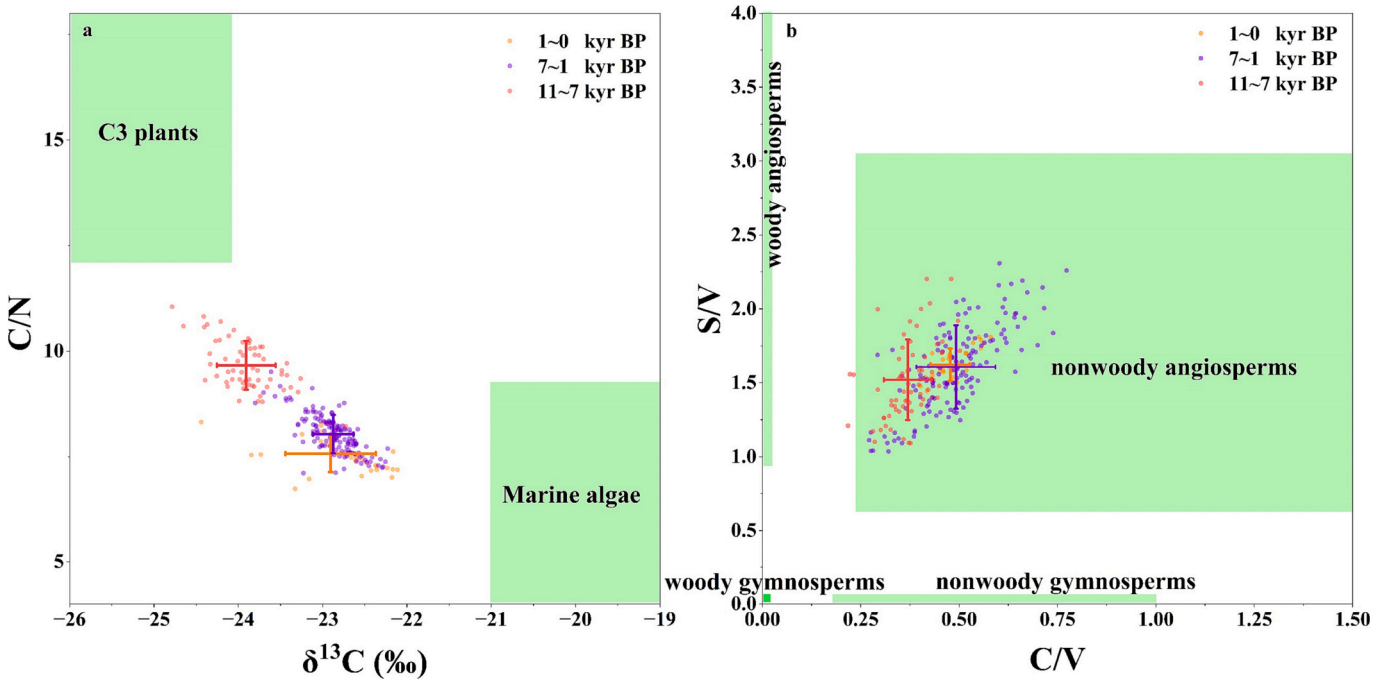

Fig. 3. a, $\delta^{13}C$ versus C/N ratio for all samples of core YS-A, the average values and standard deviation of $\delta^{13}C$ and C/N during different periods are shown, where the background labels of organic matter sources are according to Fry and Sherr (1984), Meyers (1994), Tyson (1995) and Lamb et al. (2006); b, C/V versus S/V ratios for all samples of core YS-A, the average values and standard deviation of S/V and C/V during different periods are shown, the typical ranges of different vegetation types were from Goñi et al. (1998), Bianchi et al., 2011.

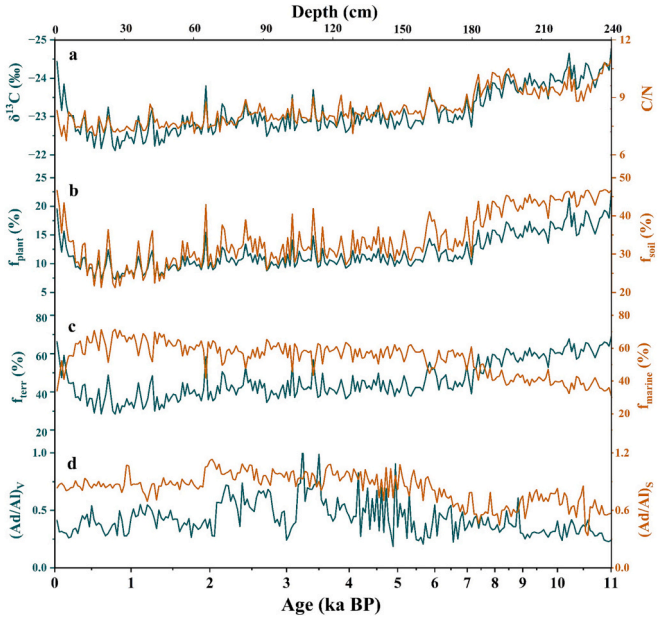

Fig. 4. Variations of organic matter proportions and degradation parameters in Core YS-A. a, $\delta^{13}C$ values (green line) and C/N (orange line) of core YS-A; b, plant OM fraction (green line) and soil OM fraction (orange line) of core YS-A; c, terrestrial OM fraction (f_{plant} and f_{soil}) (green line) and marine OM fraction (orange line) of core YS-A; d, $(Ad/Al)_V$ ratios (green line) and $(Ad/Al)_S$ ratios (orange line) of core YS-A. (For interpretation of the references to colour in this figure legend, the reader is referred to the web version of this article.)

SYSMD being a nearshore shallow sea and relatively close to the estuary, relatively low vegetation cover on the Chinese Loess Plateau triggered by cold and dry climate may be the main factor causing the reduction in terrestrial vegetation input (Fig. 5h; Wu et al., 2021; Sun et al., 2022). Based on the $\delta^{18}O$ profile of D4 in Dongge Cave, China (Dykoski et al., 2005), EASM exhibited a weaker intensity (Fig. 5i) during the early Holocene, which may resulted in lower temperatures and reduced precipitation. In addition, $(Ad/Al)_V$ and$(Ad/Al)_S$ ratios had relatively low values and increasing trend (Fig. 4d) during 11.0–7.0 ka BP, which may attributed to the increased transport distances of terrestrial input caused by rapidly increasing sea levels (Fig. 5f). After around 8.5 ka BP, Σ8 exhibited a distinct increasing trend (Fig. 5d), corresponding to the expansion of subtropical broadleaf forests (particularly angiosperms) owing to continued increase in temperature and accompanying precipitation (Hou and Fang, 2012).

During this period, the intensity of EAWM was relatively weak with fluctuations before 8.0 ka BP, and then strengthened gradually (Fig. 5j; Yancheva et al., 2007; Sone et al., 2013). It displayed a different changing tendency in the mean grain size of core YS-A (Fig. 5a), which perhaps implied that the EAWM had a relatively attenuated influence on sedimentation during this period (Zhou et al., 2015; Ai et al., 2022). Generally, rapidly rising sea levels and increased EASM may be the key factor controlling the preservation and burial of SOM in the SYSMD during 11.0–7.0 ka BP.

4.3. Climatic controls on the fate of SOM during 7.0–1.0 ka BP

The sea level at around 7.0 ka BP reached its present level and stabilized (Fig. 6e; Liu et al., 2004). The SYSMD gradually developed owing to the trapping effect of the modern circulation system since around 7.0 ka BP (Yang et al., 2003), and undergone a two-phase process of "storage in summer and transportation in winter". In summer, the discharge and loading of water and particles experience an increase due to the intensification of the summer monsoon (Liu et al., 2004; Yang et al., 2011). However, a large amount of sediment did not disperse to the nearby offshore areas, but instead accumulated in the coastal regions (Yang et al., 2011). In winter, the EAWM strengthens the currents as well as the vertical mixing process, and then breaks up the stratification formed in summer (Gong et al., 2017), resulting in that the sediments in the coastal

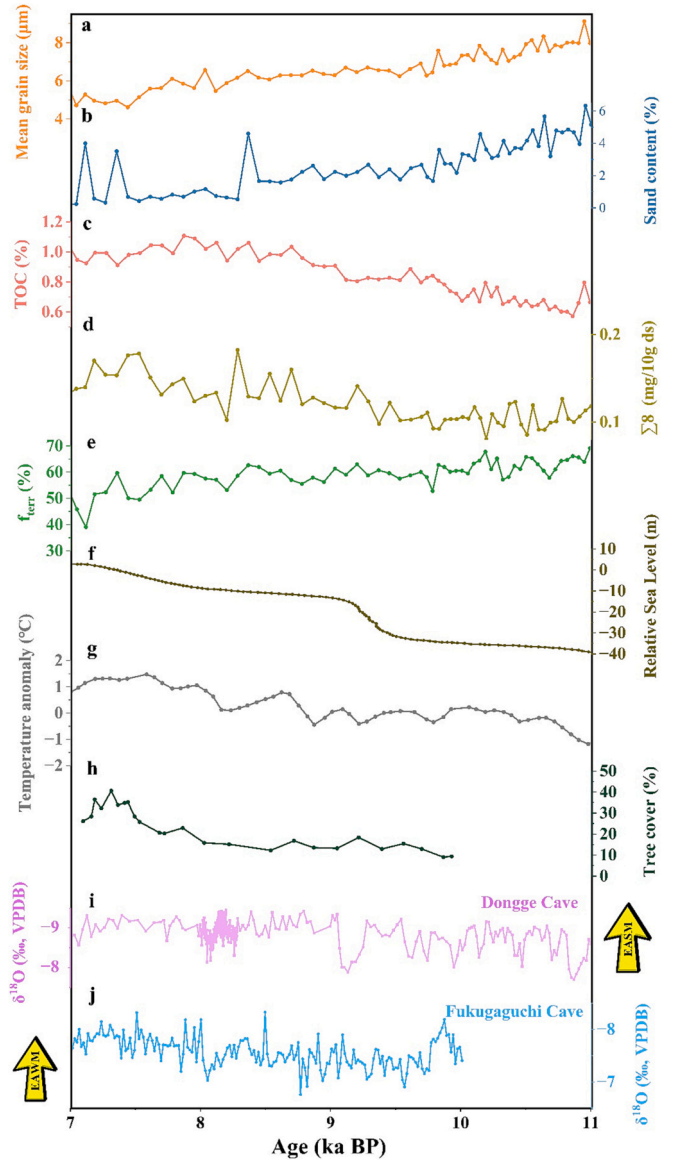

Fig. 5. Records of grain size, TOC and lignin phenols during 11.0–7.0 ka BP. a, Mean grain size core YS-A; b, sand content of core YS-A; c, TOC of core YS-A; d, Σ8 of core YS-A; e, TOM contribution of core YS-A; f, relative sea level from Yellow Sea (Liu et al., 2004); g, temperature anomaly record derived from China (Hou and Fang, 2012); h, Holocene record of tree cover from the Daihai Basin in the Loess Plateau (Sun et al., 2022); i, The $\delta^{18}O$ profile of D4 from Dongge Cave in China (Dykoski et al., 2005); j, The $\delta^{18}O$ profile of FG01 from Fukugaguchi Cave in Itoigawa (Sone et al., 2013). (For interpretation of the references to colour in this figure legend, the reader is referred to the web version of this article.)

areas accumulated in summer are resuspended and transported to the offshore areas by coastal currents such as YSCC and YSWC (Goñi and Hedges, 1995; Zhou et al., 2015). (Ad/Al)v and (Ad/Al)s ratios were relatively high during 7.0–3.0 ka BP (Fig. 4d), indicating an occurrence of higher degree of lignin degradation in the input seafloor sediments. This may be due to the warm climate and elevated temperature during this period (Fig. 6e; Hou and Fang, 2012), resulting in increased lignin degradation during transportation. Correspondingly, the sediment in core YS-A was fine-grained during 7.0–1.0 ka BP (Fig. 6a), and the TOC content and Σ8 value varied slightly with relatively high values (Fig. 6b, c). The observed phenomenon deviated from the expected pattern of temperature and tree cover decline, which can be attributed to the diminishing strength of the EASM since 7.0 ka BP (Fig. 6f). This deviation may be explained by the main source of sediments in the study area, which predominantly originates from suspended substances transported by the YSWC and YSCC during the winter since 7.0 ka BP.

Although the changes in the proxies have been relatively stable since 7.0 ka BP, phase changes still occur. The mean grain size, TOC content and Σ8 value had the similar variation trends with ENSO on millennial time scale during 7.0–1.0 ka BP (Fig. 6a–d). Notably, core YS-A was relatively coarse grained, and had relatively higher TOC content and Σ8 value (Fig. 6a–c) during 3.0–1.0 ka BP than during 7.0–3.0 ka BP, which is supported by strong statistical significance ($p < 0.05$). Meanwhile, TOC content ($r = 0.37$, $p < 0.01$) and Σ8 value ($r = 0.38$, $p < 0.01$) existed positive correlation (Fig. S5) with the variability of ENSO events during 7.0–1.0 ka BP (Fig. 6d; Haug et al., 2001; Moy et al., 2002). In addition, many other proxies such as biogenic silica, wt% Fe and sea surface temperature have been linked to the ENSO events on the millennial time scale (Barron et al., 2004; Chen et al., 2015; Nan et al., 2017; Li et al., 2021). ENSO has a significant influence on the on the current circulation (Hu et al., 2015). During an ENSO event, there was an intensification of the North Equatorial Current, which in turn enhanced the northward flow of the Kuroshio Current (Kashino et al., 2009). As a result, the YSWC, which is a branch of the northward Kuroshio Current, transported a greater amount of terrestrial material to the SYSMD (Hu et al., 2012). In addition, enhanced YSWC driven by ENSO event may have greater impact on marine productivity (Kim and Kucera, 2000; Huang et al., 2005), and thus affect the contribution of MOM (Fig. 5c). Therefore, we suggest that ENSO events may be the dominant factor controlling the fate of SOM during 7.0–1.0 ka BP.

In addition to the dominant effects of ENSO events on the millennial timescale, the SOM burial in the SYSMD is seemingly controlled by EAWM on the centennial timescale. Evidently, the sediment grain size, TOC content, and Σ8 values increased synchronously (Fig. 6a–c) during 1.1–1.5, 2.8–3.2, 4.1–4.3, 4.6–4.8, 5.1–5.3 and 5.7–6.0 ka BP, which is consistent with the four cold climate events (centennial-scale "Bond cycles" 1 to 4; Fig. 6g; Bond et al., 2001). In addition to these global cold events, our records of these proxies also revealed high value period at approximately 2.3–2.7 ka BP, which responded to the strong EAWM records of FG01 (Fig. 6g; Sone et al., 2013). This phenomenon is also reflected in other cores in the SYS (Fig. S6). During Bond events, the formation of expanded sea-ice cover over the North Atlantic and slowing of the oceanic-current conveyor system possibly enhanced the intensity of EAWM (Hao et al., 2017) and caused the entire Northern Hemisphere to experience considerably colder winters (Broecker, 2006; Wanner et al., 2008). Meanwhile, increased EAWM enhanced the strength of the coastal currents such as YSCC and YSWC, and transport more and coarser sediments form estuaries to SYSMD (Hu et al., 2012; Zhao et al., 2014), ultimately increasing TOM contribution to the SYSMD. These data indicate that Bond events-led changes in EAWM intensity may be an important factor controlling the fate of SOM in the SYSMD on the centennial time scale.

4.4. Human impacts gradually overwhelm long-term climate control on SOM deposition since 1.0 ka BP

Different from previous studies (Gong et al., 2017; Hao et al., 2017), the variation trends of TOC content, Σ8 values, and TOM contribution show a synchronous and rapidly increasing trend since 1.0 ka BP (Fig. 7a–c), which is contrary to the insignificant changes in EAWM and ENSO events (Fig. 7g). Notably, the increasing trend of these proxies were more evident after 0.4 ka BP. Simply put, the long-term climate control is inapplicable on the SOM burial in the SYSMD during this period. Similar phenomena have been observed in numerous studies and are thought to be driven by human activities (Wang et al., 2018; Chen et al., 2020; Pei et al., 2020), but their commencement times may differ. In this study, no significant differences were found in the degradation parameters, including $(Ad/Al)_V$, $(Ad/Al)_S$, and, 3,5-Bd/V, at the topmost of the core. Therefore, we believe that the influence of OM degradation

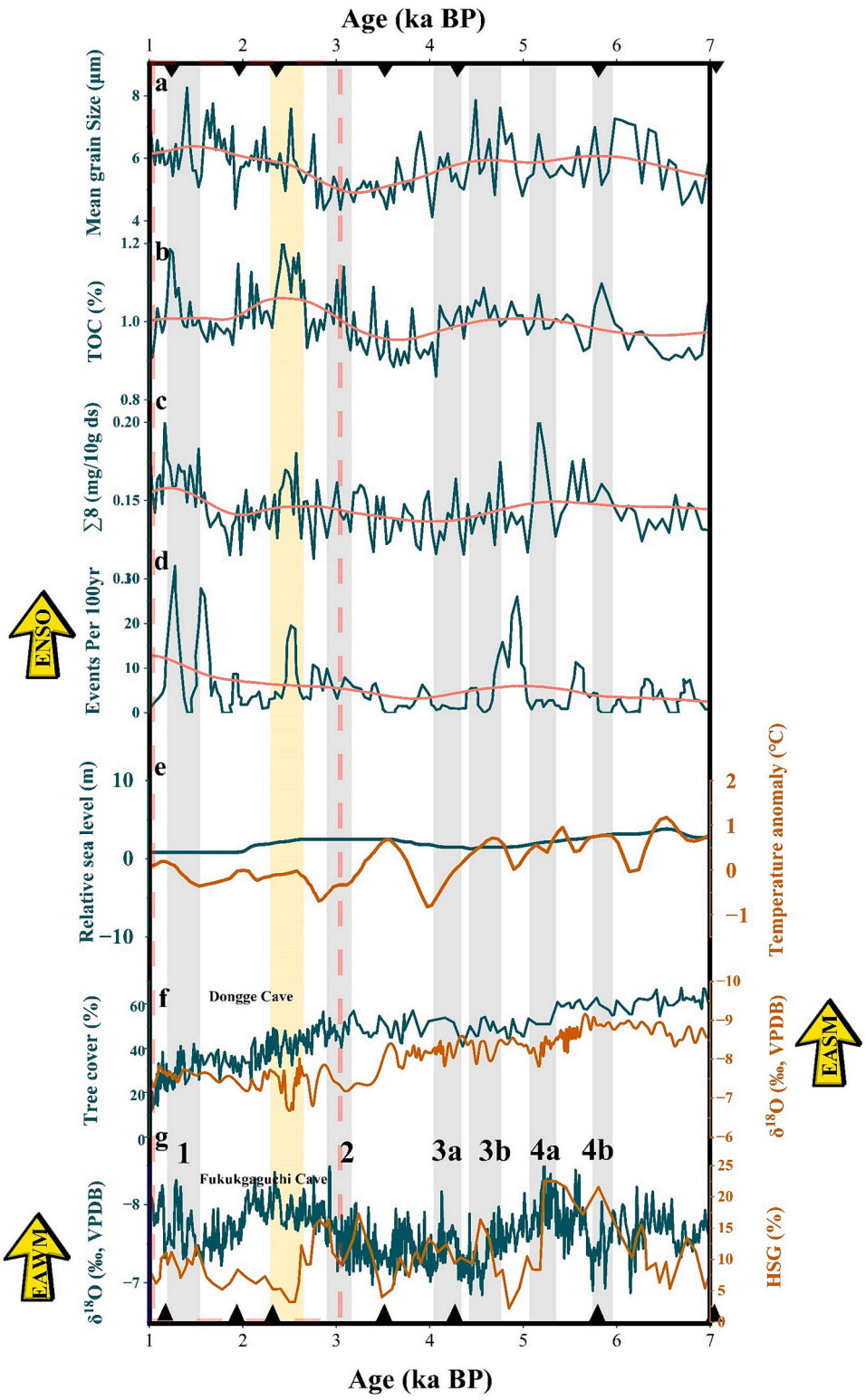

Fig. 6. Comparison of the Holocene records of grain size, TOC and lignin phenols with climate records. a, Grain size (green line) and trend line (pink line) of core YS-A; b, TOC content (green line) and trend line (pink line) of core YS-A; c, Σ8 (green line) and trend line (pink line) of core YS-A; d, ENSO events per 100 years (green line) (Moy et al., 2002) and trend line (pink line); e, relative sea level from Yellow Sea (green line) (Liu et al., 2004) and temperature anomaly record derived from China (orange line) (Hou and Fang, 2012); f, Holocene record of tree cover from the Gonghai Basin in the Loess Plateau (green line) (Sun et al., 2022) and the $\delta^{18}O$ profile of D4 from Dongge Cave in China (orange line) (Dykoski et al., 2005); g, The $\delta^{18}O$ profile of FG01 from Fukugaguchi Cave in Itoigawa (green line) (Sone et al., 2013) and cold climate events (Bond events) labeled 1 to 4 during 7.0–1.0 ka BP (orange line) (Bond et al., 2001). The red rectangles refer to changes of grain size, TOC, and Σ8 driven by the enhanced intensity and frequency of ENSO events. The grey areas refer to changes of grain size, TOC, and Σ8 driven by the strengthening trend of the EAWM intensity related to Bond events. The yellow areas refer to changes of grain size, TOC, and Σ8 driven by the other increased EAWM period. The black triangles are age control points. (For interpretation of the references to colour in this figure legend, the reader is referred to the web version of this article.)

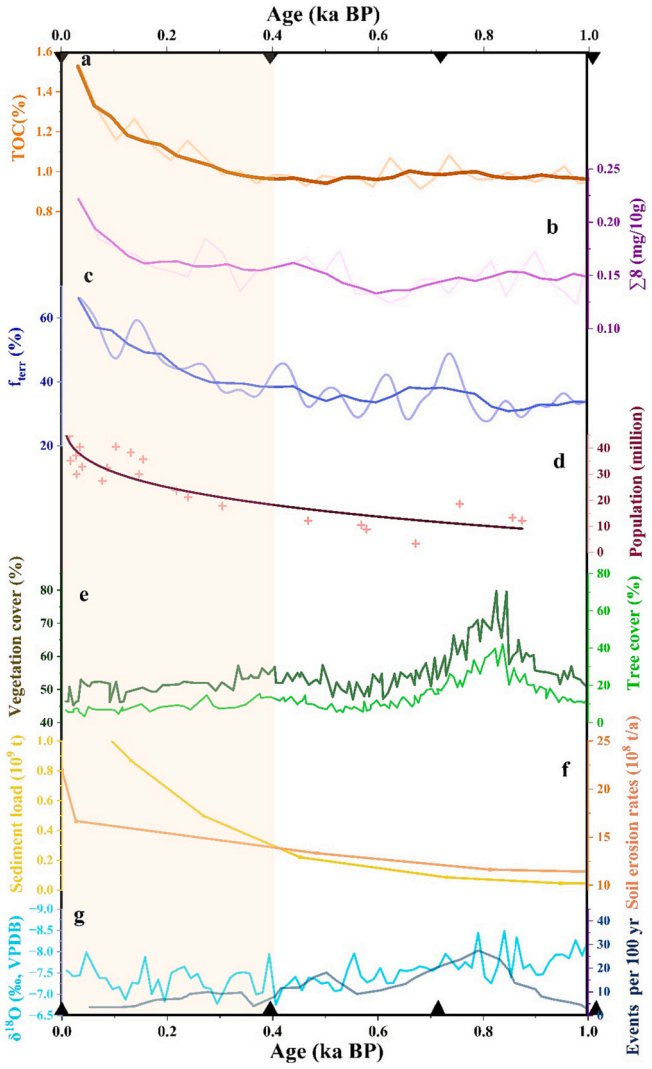

Fig. 7. Comparison of the records of TOC, Σ8 and TOM contribution with human activities records since 2.0 ka BP. a, TOC record and five points moving average of core YS-A; b, Σ8 record and five points moving average of core YS-A; c, TOM contribution record and five points moving average of core YS-A; d, Changes of population in the Loess Plateau (Zhao et al., 2013); e, Holocene record of vegetation cover (dark green line) and tree cover (light green line) from the Gonghai Basin in the Loess Plateau (Sun et al., 2022); f, Sediment load (yellow line) in the Loess Plateau (Wu et al., 2020) and soil erosion rates (orange line) in the Loess Plateau (Zhao et al., 2013); g, The $\delta^{18}O$ profile (blue line) of FG01 from Fukugaguchi Cave in Itoigawa (Sone et al., 2013) and ENSO events (purple line) per 100 years (Moy et al., 2002). The black triangles are age control points. (For interpretation of the references to colour in this figure legend, the reader is referred to the web version of this article.)

at the top of YS-A may be limited. According to historical records, early Chinese civilization developed around the Loess Plateau at the political, economic, and cultural center of China (Zhao et al., 2013). Historically, approximately 10 million people lived on the Loess Plateau at 1.0 ka BP and the population has shown an increasing trend since 1.0 ka BP (Fig. 7d; Zhao et al., 2013). During the Qing dynasty (approximately 0.3 ka BP), the population in the Loess Plateau increased relatively rapidly because of the governmental tax policies (Fig. 7d; Wang et al., 2006). TOC content ($r = 0.88$, $p < 0.01$), Σ8 values ($r = 0.86$, $p < 0.01$), TOM contribution ($r = 0.93$, $p < 0.001$), and population were found to have a positive relationship since 1.0 ka BP (Fig. S7). The rapid population growth will inevitably increase the environmental bearing pressure, thus directly changing the ecological environment of the Loess Plateau.

Following the significant growth in population, certain advanced production tools have emerged, thereby allowing for the transformation of nature. In addition, the new unified states have encouraged farmers to clear forests to expand cultivable land (Wu et al., 2020). The cultivable land area has been expanding constantly since 1.0 ka BP, with the development of population and agricultural technology (He et al., 2023). In particular, the population growth of over 25 million people during the Qianlong period of the Qing Dynasty led to the reclamation of almost all arable land, which ultimately led to the formation of an agricultural landscape (Cheng, 2010). During this period, wheat was widely cultivated in the Yellow River Basin, with wheat accounting for half of most of the northern region (Tian, 2018). According to a previous study, forest coverage was >50% during the Western Zhou dynasty (approximately 3.0 ka BP), and reduced to 40%, 33%, and 15% within the subsequent centuries (Zhao et al., 2013). By 1949, only 3–7 million ha of forestland covered nearly 6% of the Loess Plateau, mostly in the mountainous region (Zhao et al., 2013). Sun et al. (2022) indicated that both vegetation and tree covers declined significantly (Fig. 7e) with the intensification of human activities. With decreasing vegetation cover, the loess became easily erodible (Ren and Zhu, 1994), and soil erosion rates rapidly increased (Fig. 7f). Accelerated soil erosion, in addition to causing loss of topsoil as a result of soil quality degradation in an irreversible direction, also lead to catastrophic flooding events (Lal, 2003). When anthropogenic perturbation was negligible, sediment load discharged into the sea through the Yellow River was approximately 0.1–0.2 Gt/yr (Milliman et al., 1987; Saito et al., 2001), but the sediment load has been an order of magnitude higher in the last thousand years (Fig. 7f; Ren and Zhu, 1994; Saito et al., 2001; Wu et al., 2020). Furthermore, TOC content ($r = 0.76$, $p < 0.05$), Σ8 values ($r = 0.81$, $p < 0.01$), TOM contribution ($r = 0.85$, $p < 0.01$), and sediment load have shown positive correlation since 1.0 ka BP (Fig. S7). Cultivation and deforestation caused by population growth have led to the reduction in forest cover and the escalation in soil erosion, resulting in increased input of TOM during this period. These variations drastically increased the terrestrial materials exported to the sea, and resulted in higher TOM contribution to the SYSMD, thereby corresponding to the relatively high values of TOC content and Σ8 in core YS-A since 1.0 ka BP. Notably, TOC and Σ8 values had highest values since 0.4 ka BP, along with the dramatic increase in population and sediment load from the Yellow River. Therefore, human impacts have gradually overwhelmed long-term climate control on the fate of SOM since 1.0 ka BP, and this phenomenon became more evident after 0.4 ka BP.

5. Conclusions

Using the multiple proxies (grain size, bulk properties and lignin phenol index) of YS-A sediment core throughout the Holocene, this work has discussed the variations of TOM burial during different periods of Holocene, and linked its variability to climate change and human activities in the Yellow River Basin. Non-woody angiosperms dominated the TOM, and TOM in this core underwent a moderate to high degree of microbial degradation. During 11.0–7.0 ka BP, the EAWM exhibited relatively attenuated influence, sea level rise and increased EASM may be the key factors controlling the fate of SOM in the SYS. During 7.0–1.0 ka BP, the fate of SOM was controlled by ENSO events on the millennial time scale, and correlated with Bond event-led EAWM variability on the centennial time scale. Since 1.0 ka BP, TOC, Σ8, and TOM contribution has increased rapidly, contrary to the lower intensity of EAWM and ENSO events, possibly owing to the superimposition of intense human activities. Cultivation and deforestation caused by population growth have led to the reduction in forest cover and the escalation in soil erosion, resulting in increased input of TOM during this period. Therefore, anthropogenic perturbation has gradually overwhelmed long-term climate control on the fate of SOM since 1.0 ka BP, and this phenomenon became more evident after 0.4 ka BP, which providing evidence for the ongoing debate on the timing of human influence on OM burial in the

oceans.

CRediT authorship contribution statement

Chuchu Zhang: Writing – original draft, Methodology, Conceptualization. **Yifei Qiu:** Methodology, Formal analysis. **Zhi Dong:** Writing – review & editing. **Chenglong Wang:** Writing – review & editing, Funding acquisition, Conceptualization. **Yameng Wang:** Methodology. **Qihang Liao:** Methodology. **Xinqing Zou:** Writing – review & editing, Funding acquisition.

Declaration of Competing Interest

This manuscript has not been published or presented elsewhere in part or in entirety and is not under consideration by another journal. We have read and understood your journal's policies, and we believe that neither the manuscript nor the study violates any of these. There are no conflicts of interest to declare.

Data availability

Data will be made available on request.

Acknowledgement

The study was supported by the Natural Science Foundation of China (Grant Nos. 42106056), the China Postdoctoral Science Foundation (Grant Nos. 2021M691504), the Fundamental Research Funds for the Central Universities (Grant Nos. 0209-14370407) and the Innovation Project of Marine Science and Technology of Jiangsu Province (Grant Nos. JSZRHYKJ202206).

Appendix A. Supplementary data

Supplementary data to this article can be found online at https://doi.org/10.1016/j.palaeo.2023.111958.

References

Ai, L., Han, Z., Wu, X., Liu, S., Bi, N., Saito, Y., Shi, X., Wang, H., 2022. How did the climate and human activities modulate the sedimentary evolution of the Central Yellow Sea Mud, China. J. Asian Earth Sci. 235, 105299.
Andersson, A., 2011. A systematic examination of a random sampling strategy for source apportionment calculations. Sci. Total Environ. 412–413, 232–238.
Bao, R., Mcintyre, C., Zhao, M., Zhu, C., Kao, S., Eglinton, T., 2016. Widespread dispersal and aging of organic carbon in shallow marginal seas. Geology 44 (10), G37948.1.
Barron, J.A., Bukry, D., Bischoff, J.L., 2004. High resolution paleoceanography of the Guaymas Basin, Gulf of California, during the past 15 000 years. Mar. Micropaleontol. 50, 185–207.
Berner, R.A., 1982. Burial of organic carbon and pyrite sulfur in the modern ocean; its geochemical and environmental significance. Am. J. Sci. 282, 451–473.
Berner, R.A., 1990. Atmospheric carbon dioxide levels over phanerozoic time. Science 249, 1382–1386.
Bianchi, T., 2011. The role of terrestrially derived organic carbon in the coastal ocean: a changing paradigm and the priming effect. Proc. Natl. Acad. Sci. 108, 19473–19481.
Bianchi, T.S., Wysocki, L.A., Schreiner, K.M., Filley, T.R., Corbett, D.R., Kolker, A.S., 2011. Sources of terrestrial organic carbon in the Mississippi Plume Region: evidence for the importance of coastal marsh inputs. Aquat. Geochem. 17, 431–456.
Blaauw, M., Christen, J.A., 2011. Flexible paleoclimate age-depth models using an autoregressive gamma process. Bayesian Anal. 6.
Bodin, S., Meissner, P., Janssen, N.M.M., Steuber, T., Mutterlose, J., 2015. Large igneous provinces and organic carbon burial: Controls on global temperature and continental weathering during the early cretaceous. Glob. Planet. Chang. 133, 238–253.
Bond, G., Kromer, B., Beer, J., Muscheler, R., Evans, M.N., Showers, W., Hoffmann, S., LottiBond, R., Hajdas, I., Bonani, G., 2001. Persistent solar influence on North Atlantic climate during the Holocene. Science 294, 2130–2136.
Broecker, W.S., 2006. Abrupt climate change revisited. Glob. Planet. Chang. 54, 211–215.
Burdige, D.J., 2005. Burial of terrestrial organic matter in marine sediments: A re-assessment. Glob. Biogeochem. Cycles 19, GB4011.
Chen, R., Shen, J., Li, C., Zhang, E., Sun, W., Ji, M., 2015. Mid- to late-Holocene East Asian summer monsoon variability recorded in lacustrine sediments from Jingpo Lake, Northeastern China. The Holocene 25, 454–468.
Chen, F., Chen, S., Zhang, X., Chen, J., Wang, X., Gowan, E.J., Qiang, M., Dong, G., Wang, Z., Li, Y., Xu, Q., Xu, Y., Smol, J.P., Liu, J., 2020. Asian dust-storm activity dominated by Chinese dynasty changes since 2000 BP. Nat. Commun. 11.
Cheng, F., 2010. The Study on Agricultural Development of Livelihood of Shandong Province. In Nankai University, China, Tianjin.
Cuellar-Martinez, T., Ruiz-Fernández, A.C., Sanchez-Cabeza, J., Pérez-Bernal, L., López-Mendoza, P.G., Carnero-Bravo, V., et al., 2020. Temporal records of organic carbon stocks and burial rates in Mexican blue carbon coastal ecosystems throughout the Anthropocene. Glob. Planet. Chang. 192, 103215.
Deng, B., Zhang, J., Wu, Y., 2006. Recent sediment accumulation and carbon burial in the East China Sea. Glob. Biogeochem. Cycles 20, GB3014.
Dittmar, T., Lara, R.J., 2001. Molecular evidence for lignin degradation in sulfate-reducing mangrove sediments (Amazônia, Brazil). Geochim. Cosmochim. Acta 65, 1417–1428.
Dykoski, C., Edwards, R., Cheng, H., Yuan, D., Cao, Y., Zhang, M., Lin, Y., Qing, J., An, Z., Revenaugh, J., 2005. A high-resolution, absolute-dated Holocene and deglacial Asian monsoon record from Dongge Cave, China. Earth Planet. Sci. Lett. 233, 71–86.
Fry, B., Sherr, E.B., 1984. $\delta^{13}C$ measurements as indicators of carbon flow in marine and freshwater ecosystems. Contrib. Mar. Sci. 27, 13–47.
Gao, L.M., Yao, P., Wang, J.P., Zhao, B., 2016. Distribution and sources of organic carbon in surface sediments from the Bohai. Acta Oceanol. Sin. 38, 8–20 (in Chinese with English abstract).
Gong, F., Hao, T., Liu, Y., Liu, X., Zhang, D., Zhang, X., Xiang, R., Liu, Q., Li, X., 2017. Evidence for paleoclimate changes from lignin records of sediment core A02 in the southern Yellow Sea since ~ 9.5 cal. Kyr B.P. Palaeogeogr. Palaeoclimatol. Palaeoecol. 479, 173–184.
Goñi, M.A., Hedges, J.I., 1995. Sources and reactivities of marine-derived organic matter in coastal sediments as determined by alkaline CuO oxidation. Geochim. Cosmochim. Acta 59, 2965–2981.
Goñi, M.A., Ruttenberg, K.C., Eglinton, T.I., 1998. A reassessment of the sources and importance of land-derived organic matter in surface sediments from the Gulf of Mexico. Geochim. Cosmochim. Acta 62, 3055–3075.
Hao, T., Liu, X., Ogg, J., Liang, Z., Xiang, R., Zhang, X., Zhang, D., Zhang, C., Liu, Q., Li, X., 2017. Intensified episodes of East Asian Winter Monsoon during the middle through late Holocene driven by North Atlantic cooling events: High-resolution lignin records from the South Yellow Sea, China. Earth Planet. Sci. Lett. 479, 144–155.
Hartke, E.R., Cramer, B.D., Calner, M., Melchin, M.J., Barnett, B.A., Oborny, S.C., et al., 2021. Decoupling $\delta^{13}C_{carb}$ and $\delta^{13}C_{org}$ at the onset of the Ireviken Carbon Isotope Excursion: $\Delta^{13}C$ and organic carbon burial (forg) during a Silurian oceanic anoxic event. Glob. Planet. Chang. 196, 103373.
Haug, G.H., Hughen, K.A., Sigman, D.M., Peterson, L.C., Röhl, U., 2001. Southward Migration of the Intertropical Convergence Zone through the Holocene. Science 293, 1304–1308.
He, F., Yang, F., Zhao, C., Li, S., Li, M., 2023. Spatially explicit reconstruction of cropland cover for China over the past millennium. Sci. China Earth Sci. 66 (1), 111–128.
Hedges, J.I., Keil, R.G., 1995. Sedimentary organic matter preservation: an assessment and speculative synthesis. Mar. Chem. 49, 81–115.
Hedges, J.I., Blanchette, R.A., Weliky, K., Devol, A.H., 1988. Effects of fungal degradation on the CuO oxidation products of lignin: A controlled laboratory study. Geochim. Cosmochim. Acta 52, 2717–2726.
Hou, G.L., Fang, X.Q., 2012. Characteristics analysis and synthetical reconstruction of regional temperature series of the Holocene in China. J. Palaeogeogr. 14, 243–252.
Hu, B.Q., Yang, Z.S., Zhao, M.X., Saito, Y., Fan, D.J., Wang, L.B., 2012. Grain size records reveal variability of the East Asian Winter Monsoon since the Middle Holocene in the Central Yellow Sea mud area, China. Sci. China Earth Sci. 55, 1656–1668.
Hu, S., Wang, G., Wang, Q., Sprintall, J., Qu, T., Kashino, Y., Wang, F., Kessler, W.S., 2015. Pacific western boundary currents and their roles in climate. Nature 522, 299–308.
Houel, S., Louchouarn, P., Lucotte, M., Canuel, R., Ghaleb, B., 2006. Translocation of soil organic matter following reservoir impoundment in boreal systems: implications for in situ productivity. Limnol. Oceanogr. 51, 1497–1513.
Hu, L., Shi, X., Bai, Y., Qiao, S., Li, L., Yu, Y., Yang, G., Ma, D., Guo, Z., 2016. Recent organic carbon sequestration in the shelf sediments of the Bohai Sea and Yellow Sea, China. J. Mar. Syst. 155, 50–58.
Huang, D., Fan, X., Xu, D., Tong, Y., Su, J., 2005. Westward shift of the Yellow Sea warm salty tongue. Geophys. Res. Lett. 32.
Kashino, Y., España, N., Syamsudin, F., Richards, K.J., Jensen, T., Dutrieux, P., Ishida, A., 2009. Observations of the North Equatorial current, Mindanao current, and Kuroshio current system during the 2006/07 El Niño and 2007/08 La Niña. J. Oceanogr. 65, 325–333.
Kim, J., Kucera, M., 2000. Benthic foraminifer record of environmental changes in the Yellow Sea (Hwanghae) during the last 15,000 years. Quat. Sci. Rev. 19, 1067–1085.
Kim, H., Lee, H., Lee, G., 2021. New marine reservoir correction values (ΔR) applicable to dates on neolithic shells from the south coast of Koera. Radiocarbon 63, 1287–1302.
Kong, G.S., Lee, C.W., 2005. Marine reservoir corrections (△R) for southern coastal waters of Korea. The Sea 10, 124–128.
Kuzyk, Z.Z.A., Goñi, M.A., Stern, G.A., Macdonald, R.W., 2008. Sources, pathways and sinks of particulate organic matter in Hudson Bay: evidence from lignin distributions. Mar. Chem. 112, 215–229.
Lal, R., 2003. Soil erosion and the global carbon budget. Environ. Int. 29, 437–450.
Lamb, A.L., Wilson, G.P., Leng, M.J., 2006. A review of coastal palaeoclimate and relative sea-level reconstructions using $\delta^{13}C$ and C/N ratios in organic material. Earth Sci. Rev. 75, 29–57.

Li, D., Yao, P., Bianchi, T.S., Zhang, T., Zhao, B., Pan, H., et al., 2014. Organic carbon cycling in sediments of the Changjiang Estuary and adjacent shelf: Implication for the influence of three Gorges Dam. J. Mar. Syst. 139, 409–419.
Li, D., Yu, M., Jia, Y., Steinke, S., Li, L., Xiang, R., Zhao, M., 2021. Gradually cooling of the Yellow Sea warm current driven by tropical Pacific subsurface water temperature changes over the past 5 kyr. Geophys. Res. Lett. 48 e2021GL093534.
Liu, J.P., Milliman, J.D., Gao, S., Cheng, P., 2004. Holocene development of the Yellow River's subaqueous delta, North Yellow Sea. Mar. Geol. 209, 45–67.
Liu, L., Wei, G., Wang, J., Guan, Y., Wong, C.S., Wu, F., Zeng, E.Y., 2013. Anthropogenic Activities have Contributed Moderately to increased Inputs of Organic Materials in marginal Seas off China. Environ. Sci. Technol. 47, 11414–11422.
McKee, B., Aller, R., Allison, M., Bianchi, T., Kineke, G., 2004. Transport and transformation of dissolved and particulate materials on continental margins influenced by major rivers: Benthic boundary layer and seabed processes. Cont. Shelf Res. 24 (7–8), 899–926.
Meyers, P.A., 1994. Preservation of elemental and isotopic source identification of sedimentary organic matter. Chem. Geol. 114, 289–302.
Meyers, P.A., 1997. Organic geochemical proxies of paleoceanographic, paleolimnologic, and paleoclimatic processes. Org. Geochem. 27, 213–250.
Milliman, J.D., Yun-Shan, Q., Mei-E, R., Saito, Y., 1987. Man's Influence on the Erosion and Transport of Sediment by Asian Rivers: the Yellow River (Huanghe) example. J. Geol. 95, 751–762.
Moon, J., Hirose, N., Yoon, J., 2009. Comparison of wind and tidal contributions to seasonal circulation of the Yellow Sea. J. Geophys. Res. 114.
Moy, C.M., Seltzer, G.O., Rodbell, D.T., Anderson, D.M., 2002. Variability of El Niño/Southern Oscillation activity at millennial timescales during the Holocene epoch. Nature 420, 162–165.
Nan, Q., Li, T., Chen, J., Chang, F., Yu, X., Xu, Z., Pi, Z., 2017. Holocene paleoenvironment changes in the northern Yellow Sea: evidence from alkenone-derived sea surface temperature. Palaeogeogr. Palaeoclimatol. Palaeoecol. 483, 83–93.
Pei, W., Wan, S., Clift, P.D., Dong, J., Liu, X., Lu, J., Tan, Y., Shi, X., Li, A., 2020. Human impact overwhelms long-term climate control of fire in the Yangtze River Basin since 3.0 ka BP. Quat. Sci. Rev. 230, 106165.
Pellegrini, C., Tesi, T., Schieber, J., Bohacs, K.M., Rovere, M., Asioli, A., et al., 2021. Fate of terrigenous organic carbon in muddy clinothems on continental shelves revealed by stratal geometries: Insight from the Adriatic sedimentary archive. Glob. Planet. Chang. 203, 103539.
Pu, Y., Nace, T., Meyers, P.A., Zhang, H., Wang, Y., Zhang, C.L., Shao, X., 2013. Paleoclimate changes of the last 1000 yr on the eastern Qinghai–Tibetan Plateau recorded by elemental, isotopic, and molecular organic matter proxies in sediment from glacial Lake Ximencuo. Palaeogeogr. Palaeoclimatol. Palaeoecol. 379–380, 39–53.
Raven, M.R., Crockford, P.W., Hodgskiss, M.S.W., Lyons, T.W., Tino, C.J., Webb, S.M., 2023. Organic matter sulfurization and organic carbon burial in the Mesoproterozoic. Geochim. Cosmochim. Acta 347, 102–115.
Ren, M., Zhu, X., 1994. Anthropogenic influences on changes in the sediment load of the Yellow River, China, during the Holocene. The Holocene 4, 314–320.
Saito, Y., Yang, Z., Hori, K., 2001. The Huanghe (Yellow River) and Changjiang (Yangtze River) deltas: a review on their characteristics, evolution and sediment discharge during the Holocene. Geomorphology 41, 219–231.
Samper-Villarreal, J., Mumby, P.J., Saunders, M.I., Barry, L.A., Zawadzki, A., Heijnis, H., et al., 2018. Vertical accretion and carbon burial rates in subtropical seagrass meadows increased following anthropogenic pressure from European colonisation. Estuar. Coast. Shelf Sci. 202, 40–53.
Schwestermann, T., Eglinton, T.I., Haghipour, N., McNichol, A.P., Ikehara, K., Strasser, M., 2021. Event-dominated transport, provenance, and burial of organic carbon in the Japan Trench. Earth Planet. Sci. Lett. 563, 116870.
Sone, T., Kano, A., Okumura, T., Kashiwagi, K., Hori, M., Jiang, X., Shen, C., 2013. Holocene stalagmite oxygen isotopic record from the Japan Sea side of the Japanese Islands, as a new proxy of the East Asian winter monsoon. Quat. Sci. Rev. 75, 150–160.
Southon, J., Kashgarian, M., Fontugne, M., Metivier, B., Yim, W.-S., W., 2002. Marine Reservoir Corrections for the Indian Ocean and Southeast Asia. Radiocarbon 44, 167–180.
Sun, D., Tan, W., Pei, Y., Zhou, L., Wang, H., Yang, H., Xu, Y., 2011. Late Quaternary environmental change of Yellow River Basin: An organic geochemical record in Bohai Sea (North China). Org. Geochem. 42, 575–585.
Sun, Y., Zhang, S., Xu, Q., 2022. Pollen-based land cover changes reveal temporal and spatial differences of human activity in north-Central China during the Holocene. Catena 219, 106620.
Tareq, S.M., Kitagawa, H., Ohta, K., 2011. Lignin biomarker and isotopic records of paleovegetation and climate changes from Lake Erhai, Southwest China, since 18.5kaBP. Quat. Int. 229, 47–56.
Tian, H., 2018. Study on Wheat Production and Influence in the Middle and Lower Reaches of the Yellow River during the Ming and Qing Dynasty. Nanjing Agricultural University.
Tyson, R.V., 1995. Sedimentary Organic Matter: Organic Facies and Palynofacies. Chapman and Hall, London.
Wang, L., Shao, M.A., Wang, Q., Gale, W.J., 2006. Historical changes in the environment of the Chinese Loess Plateau. Environ. Sci. Pol. 9, 675–684.
Wang, X., Cui, L., Yang, S., Zhai, J., Ding, Z., 2018. Stable carbon isotope records of black carbon on Chinese Loess Plateau since last glacial maximum: An evaluation on their usefulness for paleorainfall and paleovegetation reconstruction. Palaeogeogr. Palaeoclimatol. Palaeoecol. 509, 98–104.
Wang, G., Han, J., Liu, D., 2003. The carbon isotope composition of C3 herbaceous plants in loess area of northern China. Sci. China (Series. D) 46 (10), 1069–1076.
Wang, C., Hao, Z., Gao, J., Feng, Z., Ding, Y., Zhang, C., Zou, X., 2020. Reservoir Construction has Reduced Organic Carbon Deposition in the East China Sea by half since 2006. Geophys. Res. Lett. 47.
Wang, H., Kandasamy, S., Liu, Q., Lin, B., Lou, J., Veeran, Y., Lei, H., Liu, Z., Arthur Chen, C., 2021. Roles of sediment supply, geochemical composition and monsoon on organic matter burial along the longitudinal mud belt in the East China Sea in modern times. Geochim. Cosmochim. Acta 305, 66–86.
Wang, J., Yao, P., Bianchi, T.S., Li, D., Zhao, B., Cui, X., 2015. The effect of particle density on the sources, distribution, and degradation of sedimentary organic carbon in the Changjiang Estuary and adjacent shelf. Chem. Geol. 402, 52–67.
Wang, C., Zhang, C., Wang, Y., Jia, G., Wang, Y., Zhu, C., Yu, Q., Zou, X., 2022. Anthropogenic perturbations to the fate of terrestrial organic matter in a river-dominated marginal sea. Geochim. Cosmochim. Acta 333, 242–262.
Wanner, H., Beer, J., Buetikofer, J., Crowley, T.J., Cubasch, U., Flueckiger, J., Goosse, H., Grosjean, M., Joos, F., Kaplan, J.O., Kuettel, M., Mueller, S.A., Prentice, I.C., Solomina, O., Stocker, T.F., Tarasov, P., Wagner, M., Widmann, M., 2008. Mid- to late Holocene climate change; an overview. Quat. Sci. Rev. 27, 1791–1828.
Wu, X., Xing, L., Jiang, Y., Zhang, X., Xiang, R., Zhou, L., 2019. High-resolution reconstruction of sedimentary organic matter variability during the Holocene in the mud area of the Yellow Sea using multiple organic geochemical proxies. Quat. Int. 503, 178–188.
Wu, X., Wang, H., Bi, N., Saito, Y., Xu, J., Zhang, Y., Lu, T., Cong, S., Yang, Z., 2020. Climate and human battle for dominance over the Yellow River's sediment discharge: from the Mid-Holocene to the Anthropocene. Mar. Geol. 425, 106188.
Wu, D., Zhang, C., Wang, T., Liu, L., Zhang, X., Yuan, Z., Yang, S., Chen, F., 2021. East-west asymmetry in the distribution of rainfall in the Chinese Loess Plateau during the Holocene. Catena 207, 105626.
Xing, L., Zhang, H., Yuan, Z., Sun, Y., Zhao, M., 2011. Terrestrial and marine biomarker estimates of organic matter sources and distributions in surface sediments from the East China Sea shelf. Cont. Shelf Res. 31 (10), 1106–1115.
Xu, Y., Eyles, N., Simpson, M.J., 2009. Terrigenous organic matter sources in mid Pleistocene sediments from the Orphan Knoll, Northwest Atlantic Ocean. Appl. Geochem. 24, 1934–1940.
Yancheva, G., Nowaczyk, N.R., Mingram, J., Dulski, P., Schettler, G., Negendank, J.F.W., Liu, J., Sigman, D.M., Peterson, L.C., Haug, G.H., 2007. Influence of the intertropical convergence zone on the East Asian monsoon. Nature 445, 74–77.
Yang, Z.S., Liu, J.P., 2007. A unique Yellow River-derived distal subaqueous delta in the Yellow Sea. Mar. Geol. 240 (1–4), 169–176.
Yang, S., Jung, H., Lim, D., Li, C., 2003. A review on the provenance discrimination of sediments in the Yellow Sea. Earth Sci. Rev. 63 (1), 93–120.
Yang, Z.S., Ji, Y.J., Bi, N.S., Lei, K., Wang, H.J., 2011. Sediment transport off the Huanghe (Yellow River) delta and in the adjacent Bohai Sea in winter and seasonal comparison. Estuar. Coast. Shelf Sci. 93, 173–181.
Yoneda, M., Uno, H., et al., 2007. Radiocarbon marine reservoir ages in the western Pacific estimated by pre-bomb molluscan shells. Nucl. Inst. Methods Phys. Res. B 259, 432–437.
Yu, H., Wu, Y., Zhang, J., Yao, Q.Z., Zhu, Z.Y., 2007. The characteristics of lignin of plants and soil samples in the Yangtze River (Changjiang) drainage basin. Acta Scientiae Circumstantiae 27, 817–823 (in Chinese with English abstract).
Yu, H., Wu, Y., Zhang, J., Deng, B., Zhu, Z.Y., 2011. Impact of extreme drought and the three Gorges Dam on transport of particulate terrestrial organic carbon in the Changjiang (Yangtze) river. J. Geophys. Res. 116, F04029.
Yuan, D., Zhu, J., Li, C., Hu, D., 2008. Cross-shelf circulation in the Yellow and East China Seas indicated by MODIS satellite observations. J. Mar. Syst. 70, 134–149.
Zhang, T., 2012. Sedimentary records of lignin in Yellow Sea and East China Sea and the application to the study of fate of terrestrial organic carbon and environmental changes. Ocean University of China.
Zhao, G., Mu, X., Wen, Z., Wang, F., Gao, P., 2013. Soil erosion, conservation, and eco-environmental changes in the Loess Plateau of China. Land Degrad. Dev. 24, 499–510.
Zhang, J., Wu, Y., Jennerjahn, T.C., Ittekkot, V., He, Q., 2007. Distribution of organic matter in the Changjiang (Yangtze River) Estuary and their stable carbon and nitrogen isotopic ratios: Implications for source discrimination and sedimentary dynamics. Mar. Chem. 106, 111–126.
Zhao, M.X., Ding, L., Xing, L., Qiao, S.Q., Yang, Z.S., 2014. Major mid-late Holocene cooling in the East China Sea revealed by an alkenone sea surface temperature record. J. Ocean Univ. China. 13, 935–940.
Zhao, B., Yao, P., Bianchi, T.S., Yu, Z.G., 2021. Controls on Organic Carbon Burial in the Eastern China marginal Seas: A Regional Synthesis. Glob. Biogeochem. Cycles 35.
Zhou, C., Dong, P., Li, G., 2015. Hydrodynamic processes and their impacts on the mud deposit in the Southern Yellow Sea. Mar. Geol. 360, 1–16.